



Heriot-Watt University  
Research Gateway

## A new multi-pore fractal model to delineate the effect of various factors on imbibition in shales

### Citation for published version:

Zhao, Z, Jiang, Z, Guo, J, He, S & Chen, C 2021, 'A new multi-pore fractal model to delineate the effect of various factors on imbibition in shales', *Fuel Communications*, vol. 7, 100012.  
<https://doi.org/10.1016/j.fueco.2021.100012>

### Digital Object Identifier (DOI):

[10.1016/j.fueco.2021.100012](https://doi.org/10.1016/j.fueco.2021.100012)

### Link:

[Link to publication record in Heriot-Watt Research Portal](#)

### Document Version:

Publisher's PDF, also known as Version of record

### Published In:

Fuel Communications

### Publisher Rights Statement:

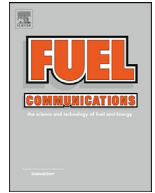
© 2021 The Author(s). This is an open access article under the CC BY-NC-ND license.

### General rights

Copyright for the publications made accessible via Heriot-Watt Research Portal is retained by the author(s) and / or other copyright owners and it is a condition of accessing these publications that users recognise and abide by the legal requirements associated with these rights.

### Take down policy

Heriot-Watt University has made every reasonable effort to ensure that the content in Heriot-Watt Research Portal complies with UK legislation. If you believe that the public display of this file breaches copyright please contact [open.access@hw.ac.uk](mailto:open.access@hw.ac.uk) providing details, and we will remove access to the work immediately and investigate your claim.



# A new multi-pore fractal model to delineate the effect of various factors on imbibition in shales

Zhihong Zhao<sup>a,\*</sup>, Zeyun Jiang<sup>b</sup>, Jianchun Guo<sup>a</sup>, Songgen He<sup>c</sup>, Chaogang Chen<sup>d</sup>

<sup>a</sup> State Key Laboratory of Oil and Gas Reservoir Geology and Exploitation, Southwest Petroleum University, Chengdu 610500, China

<sup>b</sup> IGE/EGIS Herriot-Watt university, Edinburgh EH14 4AS, United Kingdom

<sup>c</sup> Petroleum Engineering Technology Institute of Southwest Oil & Gas Company, SINOPEC, Deyang 618099, China

<sup>d</sup> Chongqing Shale gas Exploration and Development Co. LTD, Chongqing 401121, China

## ARTICLE INFO

### Article history:

Received 29 August 2020

Revised 6 March 2021

Accepted 10 March 2021

### Keywords:

Multiple pores

Fractal model

Imbibition model

Shale

## ABSTRACT

Large-scale hydraulic fracturing of horizontal wells is a key technology for shale gas extraction, during which tens of thousands of cubic meters of water could be injected into the formations for hydraulic fracturing. Water is imbibed into the shale pores under the action of capillary force and osmotic pressure. The relevant research has intensively been conducted worldwide on imbibition in porous media, including fractal modeling of the phenomenon. One significant drawback of the imbibition models proposed is their focus solely on the capillary force and pore fractal characteristics, ignoring the self-imbibition of clay pores under osmotic pressure. In this paper, the pore characteristics of shale are analyzed by field emission scanning electron microscopy (FSEM) and fractal analysis. A multi-pore fractal model is then developed for imbibition in shales, honoring capillary forces, osmotic pressure and pore structure. The results show that the morphology of organic and brittle pores tends to resemble an ellipse, while that of clay pores is similar to parallel fractures. It is observed that the imbibition capacity is more influenced by the fractal dimension of pore tortuosity rather than pore volume. In this regard, the effect of the maximum short axis of an elliptic pore on imbibition is more important than that of the minimum short axis. The imbibition ability has a direct relationship with fluid viscosity. But there is a critical viscosity value, beyond which the imbibed volume flattens out. In the case of multiple-pore imbibition, clay pores demonstrate the fastest, longest and largest liquid imbibition process.

© 2021 The Author(s). Published by Elsevier Ltd.  
This is an open access article under the CC BY-NC-ND license  
(<http://creativecommons.org/licenses/by-nc-nd/4.0/>)

## 1. Introduction

The typical shale porous system can be characterized as one with extremely narrow pore throats, multiple coexisting pore types, low porosity, high degrees of compactness, large specific surface area, complex minerals, organic matter, natural cracks and weakly cemented [1–4]. Massive hydraulic fracturing has become an essential technology for commercial exploitation of shale gas [5–7]. Extensive fracturing in horizontal wells can interconnect natural cracks and fractures, creating new gas flow networks near the wellbore [8–10]. Ten thousand cubic meters of water-based fracturing fluid can be injected into shale formations during hydraulic fracturing [11]. Because of the disparity in geological characteristics of the fractured area (compared to the original reservoir

conditions) and in fracturing fluid performance, the fracturing fluid typically has low flowback rate in shale reservoirs. Representative values are shown in Table 1. Upon fracturing, there is an inverse correlation between gas production and flowback rate; in fact, a “V” shape is observed in the flowback gas-to-water ratio [12,13]. This can be explained by the suction of a large volume of the injected fluid into the shale nano-pores through the action of capillary forces and osmotic pressure [14,15].

To describe water imbibition, Handy [20] assumed that the process is a piston-like displacement, the flow obeys the Darcy's Law and the pressure gradient of the gas phase at the leading edge of the water phase could be ignored, thus obtaining a one-dimensional imbibition model. Li and Horne [21] established a linear model between the self-imbibition rate and the reciprocal of the self-imbibition volume based on the Handy model. Li and Horne [22] improved the imbibition model by taking the original saturation into account. In fact, these models are based on uniform capillary bundle and are unable to effectively describe the

\* Corresponding author.

E-mail address: [swpuzzh@163.com](mailto:swpuzzh@163.com) (Z. Zhao).

**Table 1**  
Flowback rate after shale fracturing in five North America and four China projects.

Region	Formation	Flowback rate (%)
North America	Barnet/Marcelus [16]	50
	Horn River [17]	25-55
	Haynesville [16]	5
	Eagle Ford [18]	<20
	Average in North America [19]	6-10
China	Weiyuan	40.3
	Yongchuan	34.3
	Changning	12.7
	Fuling	3.9

fluid flow in shale [23]. However, the shale pore size spans a large range of length scales from nanometer to micron, for instance, so the uniform capillary bundle model is not suitable for modeling fluid flow in shale rocks. Nevertheless, the fractal theory was suggested [24,25] to be sufficiently powerful to characterize disorder and irregular objects in shale. Based on the models presented by Li and Horne, Li and Zhao [26] employed the fractal theory to propose a fractal power law for the relationship between imbibition rate and time.

Lucas [27] and Washburn [28] established the LL-W model with circular capillaries as pore channels under the assumptions of quasi-equilibrium conditions and a Newtonian-fluid laminar flow, governed by hydrostatic pressure and capillary forces. Based on this model, Zhmud et al. [29] deduced the asymptotic solution of the vertical capillary. Fries and Dreyer [30] calculated the self-imbibition of the inclined capillary based on the LL-W model. Furthermore, Benavente et al. [31] and Dimitrov et al. [32] improved the LL-W model by incorporating tortuous pores with specific shape factors and slip length, accounting for the slip phenomenon during imbibition, respectively. Recently, Cai and Yu [24] utilized the fractal theory to quantify pore characteristics of porous media. They adopted the general idea behind the L-W model to establish a fractal imbibition model driven by both capillary and gravity forces.

The models mentioned above take only capillary force into consideration, neglecting the effect of osmotic pressure that is a driving force of imbibition. Multiple pore types are associated with shale such as brittle, organic and clay pores. The clay pores act similar to semi-permeable membranes and their poor mineralization leads to osmotic pressure [48]. Therefore, it is reasonable and necessary to include osmotic pressure in models of imbibition. In this paper, we develop a fractal imbibition model for shale rocks that accounts for the two forces mentioned as well as multiple pore types.

## 2. Three types of shale pores

Quanta250 FEG field emission scanning electron microscope (FESEM) has been widely utilized to reveal pore characteristics in shale rocks [33]. The instrument is able to reach imaging and backscattering electron imaging resolutions of up to 1.2 nm and 2.5 nm, respectively. The scanner is also powered by an INCA-MAX20 type energy spectrometer to allow micro-region composition analysis. To study nanoscale pores, such as organic pores in shale, argon ion polishing can be used to crop off thin cross sections from bulk samples.

Fig. 1 shows FESEM images of the three shale pore types, captured from the samples in Longmaxi shale formation in Sichuan, China. As illustrated, organic pores are roughly round or oval in shape (Fig. 1A); clay pores are narrow slits relatively high in width and length (Fig. 1C); and the brittle mineral pores can be described as mainly irregular polygons (Fig. 1B).

Statistical average was performed for various pore sizes in FESEM images, the pore length-width ratios for organic and brittle mineral pores are 2.336 and 3.286, respectively, which can point to an elliptic shape. On the other hand, the average ratio for clay pores is 4.397, which is close to that of parallel fractures. As observed in many experiments [34-36], this analysis also confirms that shale pores can be characterized either by elliptic pores or by micro-fractures.

Fig. 2 presents pore size distributions of the three pore types occurring in the Longmaxi samples. Note that the presence of organic and clay pores is visually evident in the range of 10 and 30 nm, while brittle mineral pores are most frequently rendering at 100 to 200 nm. These main distribution ranges of different pore diameters are consistent with previous findings [37,38].

## 3. Multiple-pore shale imbibition model

Based on the discussions presented in Section 2, the process of imbibition in shales can be decomposed into two distinct regimes:

- (1) Imbibition in organic and brittle mineral pores (non-clay pores), resembling an elliptic tube with a long axis  $a$ , and a short axis  $b$  (Fig. 3A);
- (2) Imbibition in clay pores, similar to a fracture with a width of  $w$  (Fig. 3B).

### 3.1. Imbibition model for non-clay pores

As aforementioned, non-clay pores (organic and brittle mineral pores) are similar to ellipses in shape. The fluid laminar flows in an elliptic tube, as a model of a nanopore channel [39], can be schematically illustrated in Fig. 4.

For laminar flow of incompressible and viscous fluid through an elliptic tube, the simplified Navier-Stokes (N-S) equation can be applied to characterize the flow in such an elliptic tube:

$$\frac{\partial^2 u}{\partial y^2} + \frac{\partial^2 u}{\partial z^2} = \frac{1}{\mu} \frac{dp}{dx} \quad (1)$$

where  $p$  is the differential pressure and  $u$  and  $\mu$  are the aqueous phase velocity and viscosity, respectively. Since the velocity is at its maximum at the center of the ellipse, the velocity gradient is zero at this point. Therefore, the following boundary conditions apply to the N-S equation:

$$\begin{cases} y = 0, z = 0, \frac{\partial u}{\partial y} = 0 \\ y = 0, z = 0, \frac{\partial u}{\partial z} = 0 \end{cases} \quad (2)$$

Many experiments [e.g., 32,40,41] have verified that the boundary slip effect cannot be ignored when the fluid flows in pore channels at micro- or nano-meter scale, and the no-slip boundary condition is valid any more for shale rocks [42]. While the liquid flow within the shale pores is subject to slippage near the boundary (Fig. 5), the N-S equation can still describe the flow [43].

Further to Eq. (2), an additional boundary condition is defined by Eq. (3):

$$\begin{cases} u = -L_s \frac{\partial u}{\partial y} |_{y=b, z=0} \\ u = -L_s \frac{\partial u}{\partial z} |_{z=a, y=0} \end{cases} \quad (3)$$

where  $a$  is the long axis of the elliptic pore,  $b$  is the short axis and  $L_s$  is the boundary slip length (Fig. 5b). Eq. (1) can be solved if the boundary conditions in a straight elliptic tube is considered:

$$q = \frac{\pi m^2 b^3 [mb^2 + 6(m+1)bL_s + 32L_s^2] \Delta p}{64\mu[(m^2+1)b + 4(m+1)L_s] L} \quad (4)$$

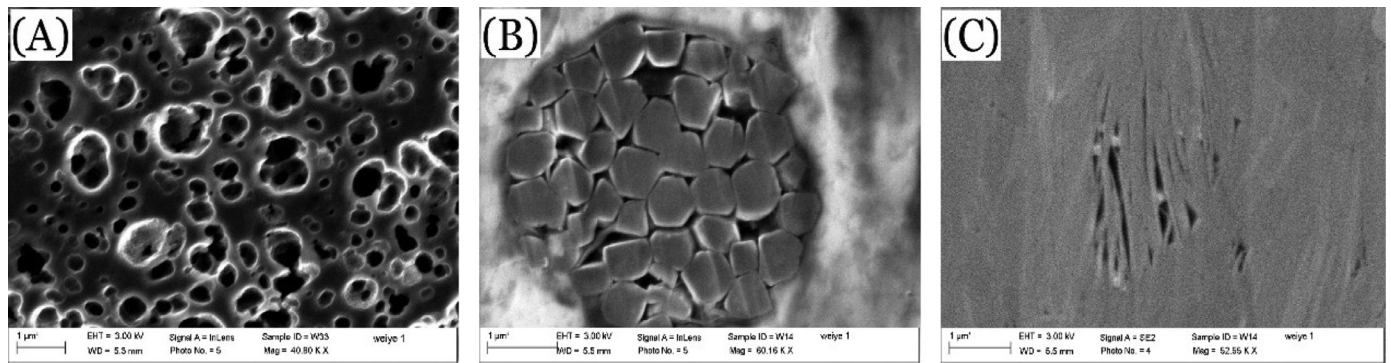


Fig. 1. Three types of pores in shale: organic (A), brittle mineral (B) and clay (C) pores. Shale rocks collected from Longmaxi shale formation in Sichuan, China.

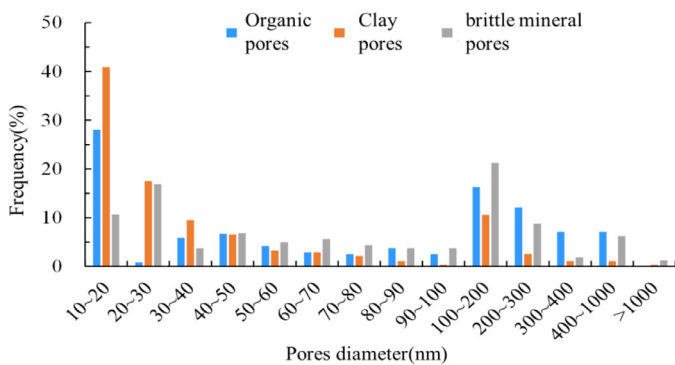


Fig. 2. Distribution of different types of pores in the Longmaxi shale samples.

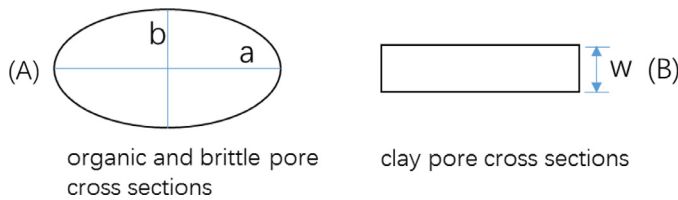


Fig. 3. Schematic diagrams of equivalent pore cross sections in shale: non-clay pores (A) and clay pores (B).

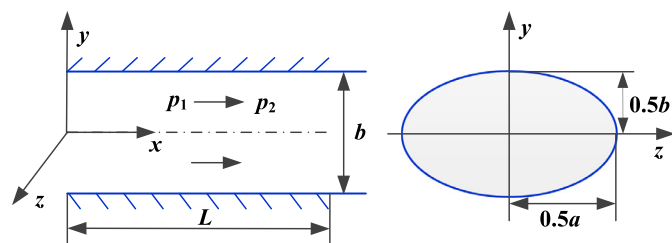


Fig. 4. Schematic diagram of laminar flow in a circular tube.

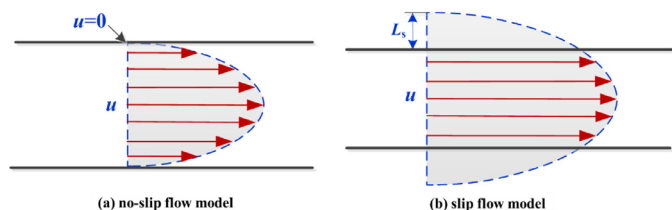


Fig. 5. The schematic diagram of boundary condition without (a) and with (b) slip-page.

where  $q$  is flow rate,  $m$  is the aspect ratio of elliptical pores ( $a/b$ ) and  $L$  is the length of the fluid imbibed into the elliptic tube. Eq. (4) describes imbibition in a straight single elliptic tube. However, an actual shale porous system is characterized by heterogeneity and randomness, the simplest representation of which is tortuosity. Based on the fractal theory, tortuous streamline in an elliptic tube can be described by Yu & Cheng [44]:

$$L_t(d) = b^{1-D_T} L^{D_T} \tag{5}$$

Where  $D_T$  is the flexibility fractal dimension and  $L_t$  is actual streamline length. If capillarity is considered as the dominant driving force for imbibition in shales, ignoring gravity [45], the shale imbibition pressure drop can be given by:

$$\Delta p = 2\sigma \left( \frac{\cos \theta}{mb} + \frac{\cos \theta}{b} \right) \tag{6}$$

Where  $\sigma$  is the gas-water interfacial tension and  $\theta$  is wetting contact angle. By substituting Eq. (5) and (6) into Eq. (4), an equation for tortuous elliptic-pore imbibition can be obtained:

$$q = \frac{\pi m(m+1)\sigma b^{1+D_T} \cos \theta [mb^2 + 6(m+1)bL_s + 32L_s^2]}{32\mu [(m^2+1)b + 4(m+1)L_s] L_o^{D_T}} \tag{7}$$

Where  $L_o$  is the imbibition length that is the length of fluid sucked in non-clay pores. The drawback of this equation is that it only considers a single elliptic pore, in reality shale is a multi-pore medium. The fractal scaling of elliptic pore size can be expressed by Li [46]:

$$-dN = D_f b_{max}^{D_f} b^{-(D_f+1)} db \tag{8}$$

Where  $D_f$  is the fractal dimension,  $b_{max}$  is the maximum pore diameter (i.e., the biggest of all non-clay pores in a shale sample) and  $N$  is the number of fractal elements. The total flow can be obtained using Gauss-Legendre integral for all elliptic pores based on Eq. (7) and (8):

$$\begin{cases} Q = \frac{\pi m(m+1)\sigma \cos \theta D_f b_{max}^{D_f} (b_{max} - b_{min})}{64\mu L^{D_f}} \sum_{k=0}^n \omega_k \left\{ \frac{b_k^{D_f - D_T} [mb_k^2 + 6(m+1)L_s b_k + 32L_s^2]}{(m^2+1)b_k + 4(m+1)L_s} \right\} \\ b_k = \frac{b_{max} - b_{min}}{2} t_k + \frac{b_{max} + b_{min}}{2} \end{cases} \tag{9}$$

Where  $b_{min}$  is the smallest diameter of all non-clay pores in a shale,  $\omega_k$  is the weight coefficient,  $n$  is the number of segments in the Gauss integral formula and  $t_k$  is the Gauss point determined by  $n$ . For example,  $n = 4$ ,  $t_k = \pm 0.8611363, \pm 0.3399810$  and  $\omega_k = 0.3478548, 0.6521452$ . According to the Sierbinsi carpet fractal model [47], the total pore area per unit is:

$$A_p = \frac{\pi m b_{max}^2 D_f (1 - \phi)}{4(2 - D_f)} \tag{10}$$

**Table 2**  
The measured parameters for non-clay pore imbibition modeling.

Parameter	$\theta$	$\mu$	$\sigma$	$L_s$	$m$	$D_f$	$D_T$	$b_{max}$	$b_{min}$
Unit	$^\circ$	$mPa\cdot s$	$mN/m$	$nm$	-	-	-	$nm$	$nm$
Value	30	1	70	0	1	1.62	1.269	3230	1.49

where  $\Phi$  is the total porosity of shale. Thus, the average velocity of all curved capillary tubes can be derived as:

$$\bar{v}_t = \frac{Q}{A_p} = \frac{\sigma \cos \theta b_{max}^{D_f-2} (m+1)(2-D_f)(b_{max}-b_{min})}{16\mu(1-\phi)L^{D_T}} \times \sum_{k=0}^n \omega_k \left\{ \frac{b_k^{D_T-D_f} [mb_k^2 + 6(m+1)L_s b_k + 32L_s^2]}{(m^2+1)b_k + 4(m+1)L_s} \right\} \quad (11)$$

On the other hand, the average flow velocity of all curved capillary tubes can also be obtained by integrating both sides of Eq. (6) after differentiation [47]:

$$\bar{v}_t = \frac{D_T D_f}{D_T + D_f - 1} b_{min}^{1-D_T} L^{D_T-1} v_0 \quad (12)$$

Combining Eq. (11) and (12), and integrating with respect to time  $t$  results in the following equation for the imbibition length of non-clay elliptic pores:

$$L = \left\{ \frac{\sigma \cos \theta b_{max}^{D_f-2} (m+1)(2-D_f)(D_T + D_f - 1)(b_{max}-b_{min})}{8\mu D_f b_{min}^{1-D_T} (1-\phi)} \times \sum_{k=0}^n \omega_k \left\{ \frac{b_k^{D_T-D_f} [mb_k^2 + 6(m+1)L_s b_k + 32L_s^2]}{(m^2+1)b_k + 4(m+1)L_s} \right\} \right\}^{\frac{1}{2D_T}} \frac{1}{t} \frac{1}{2D_T} \quad (13)$$

Although imbibition in organic or brittle mineral pores could be described by this equation, the final imbibition volume should take both pore types into account. Assuming the contact area between shale and liquid is  $A_{im}$ , the imbibition volume of elliptical pores in shale hence is:

$$V_{imn} = V_{imo} + V_{imb} = A_{im}(\phi_{to}L_o + \phi_{tb}L_b) \quad (14)$$

Where  $V_{imn}$ ,  $V_{imo}$  and  $V_{imb}$  are the imbibition volume of non-clay pores, organic pores and the brittle pores, respectively;  $A_{im}$  is the contact area of fluid and shale; subscripts  $o$  and  $b$  represent organic and brittle mineral pores;  $\Phi_{to}$  and  $\Phi_{tb}$  are porosities from the organic and brittle mineral pore; and finally  $L_o$  and  $L_b$  are the imbibition length of organic pores and brittle mineral pores.

For elliptic tubes, its length-width ratio is 1, the model (Eq. (13)) can be simplified as an imbibition model. Furthermore, if the slip length is zero, the model is then consistent with the fractal imbibition model given by Cai et al. [24]. Using the measured properties as listed in Table 2, we can calculate imbibition volumes by both models and are able to confirm the excellent agreement as illustrated in Fig. 6, which validates our model in a comparative sense.

### 3.2. Imbibition model for clay pores

Compared with non-clay pores, the clay surface is charged, and the osmotic pressure can then be generated due to the effect of double electron layers and the difference of salinity between inside and outside the formation [48]. Therefore, the forces exerted on clay pores during self-imbibition should include not only capillary force but also osmotic pressure. The osmotic pressure is often calculated by Van 't Hoff's formula [49].

$$p_\pi = \varepsilon E_\pi RT (C_{sh} - C_f) \quad (15)$$

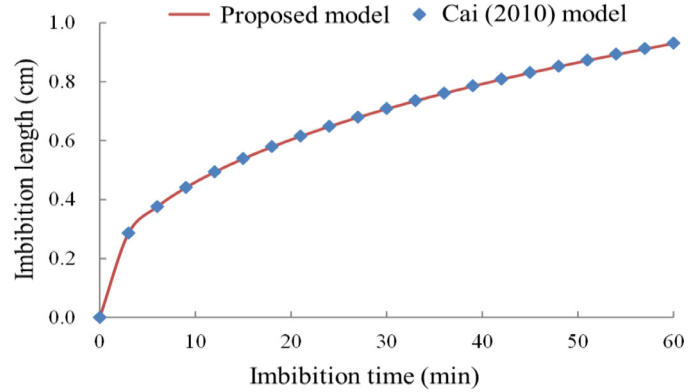


Fig. 6. Comparison of two non-clay pore imbibition models.

Where  $p_\pi$  is the osmotic pressure,  $\varepsilon$  is the number of ions after solute ionization,  $E_\pi$  is the membrane efficiency,  $R$  is the gas constant of 0.08206,  $T$  is the absolute temperature of a formation,  $C_{sh}$  is the molar solute concentration in the original formation water and  $C_f$  is the molar solute concentration in the fracturing fluid. And the calculation formula of  $E_\pi$  is [49].

$$E_\pi = 1 - \frac{(R_{ca-w} + 1)C_a/C_s}{\{R_{ca-w}(C_a/C_c) + 1 + R_{a-mw}[R_{ca-m}(C_a/C_c) + 1]\}\Phi_c} \quad (16)$$

$$\begin{cases} C_s = \frac{1}{2}(C_f + C_{sh}) \approx \frac{1}{2}C_{sh} \\ C_a = -\frac{1}{2}E_{CEC}\rho_{clay}(1-\phi_c) + \frac{1}{2}[E_{CEC}^2\rho_{clay}^2(1-\phi_c)^2 + 4C_s^2\phi_c^2]^{\frac{1}{2}} \\ C_c = C_a + E_{CEC}\rho_{clay}(1-\phi_c) \end{cases} \quad (17)$$

Where  $E_{CEC}$  is the cation exchange capacity of shale;  $R_{ca-w}$  is the ratio of the friction coefficients of anions to water;  $R_{ca-m}$  is the ratio of the friction coefficients of anions to membrane;  $R_{a-mw}$  is the ratio of the friction coefficients of anion semi-permeable membrane to cation water;  $C_a$  is the concentration of anions in the pores of the semi-permeable membrane;  $C_s$  is the arithmetic mean of solute in solution on both sides of the semi-permeable membrane;  $C_c$  is the cationic concentration in the semi-permeable film;  $\Phi_c$  is the clay mineral porosity; and finally,  $\rho_{clay}$  is the density of clay minerals.

As the clay pore imbibition mainly caused by the action of capillary force and osmotic pressure, so the difference of self-imbibition pressure is the sum of these two pressures, which can be described by:

$$\Delta p = \frac{2\sigma \cos \theta}{w} + \varepsilon E_\pi RT (C_{sh} - C_f) \quad (18)$$

Where  $w$  is clay pore width. On the basis of the plate flow equation [50] and including the boundary slip, the parallel plate flow equation can be given by:

$$q = \frac{Bw^3}{12\mu} \frac{\Delta p}{L} \left(1 + \frac{6L_s}{w}\right) \quad (19)$$

Where  $B$  is the length of the clay pores. On the other hand, the parallel plate flow rate has the following relationship with time:

$$q = Bw \frac{dL}{dt} \quad (20)$$

By fusing together Eq. (18-20), the imbibition length of a single clay pore can be obtained as:

$$L = \sqrt{\frac{\sigma \cos \theta}{3\mu} (w + 6L_s) + \frac{\varepsilon E_o RT (C_t - C_f)}{6\mu} (w^2 + 6L_s w)} \cdot \sqrt{t} \quad (21)$$

As all the pores are at nano-scale, the fractal statistical properties of circular pores are still applicable to clay pores. Eq. (5) can be modified to replace the pore diameter of the elliptic tube by clay pore width that is  $w$ . By doing so, the tortuous streamline of the clay pores can be related to the straight-line distance as:

$$L_t(w) = w^{1-D_T} L^{D_T} \quad (22)$$

Eq. (20) and (21) can be combined to give the imbibition flow rate of a single curved capillary:

$$q = \frac{\xi \sigma \cos \theta}{6\mu} \frac{1}{L^{D_T}} (w^{2+D_T} + 6L_s w^{1+D_T}) + \frac{\xi}{12\mu} \frac{p_\pi}{L^{D_T}} (w^{3+D_T} + 6L_s w^{2+D_T}) \quad (23)$$

The expression formula of the elliptic fractal (Eq. (8)) can also be applied to clay pores:

$$-dN = D_f W_{\max}^{D_f} w^{-(D_f+1)} dw \quad (24)$$

Combined with Eq. (24), the single clay pore flow formula (Eq. (23)) can be integrated over all clay pores to calculate the total imbibition rate. This would lead to the actual average curved clay pore flow rate:

$$\bar{v}_t = \frac{Q}{A_p} = \frac{2 - D_f}{(1 - \phi)} \left[ \frac{\sigma \cos \theta}{6\mu} \frac{1}{L^{D_T}} (A_2 + 6L_s B_2) + \frac{p_o}{12\mu} \frac{1}{L^{D_T}} (C_2 + 6L_s A_2) \right] \quad (25)$$

Where the unknown parameters are given by:

$$A_2 = \frac{w_{\max}^{D_{Tc}} (1 - \beta_c^{2+D_{Tc}-D_{fc}})}{2 + D_{Tc} - D_{fc}} \quad (26)$$

$$B_2 = \frac{w_{\max}^{D_{Tc}-1} (1 - \beta_c^{1+D_{Tc}-D_{fc}})}{1 + D_{Tc} - D_{fc}} \quad (27)$$

$$C_2 = \frac{w_{\max}^{1+D_{Tc}} (1 - \beta_c^{1+D_{Tc}-D_{fc}})}{3 + D_{Tc} - D_{fc}} \quad (28)$$

$$\beta_c = \frac{w_{\min}}{w_{\max}} \quad (29)$$

In Eq. (29),  $w_{\max}$  and  $w_{\min}$  are the maximum and minimum clay pore widths, respectively;  $\beta_c$  is the ratio of the  $w_{\min}$  and  $w_{\max}$ ; the subscript  $c$  refers to clay pore. Upon integration with respect to time, Eq. (25) can be used to compute the imbibition length in clay pores:

$$\begin{cases} L_c = L_{cp} + L_\pi \\ L_{cp} = \left\{ \frac{(D_T+D_f-1)(2-D_f)}{D_f w_{\min}^{1-D_T} (1-\phi)} \left[ \frac{\sigma \cos \theta}{3\mu} (A_2 + 6L_s B_2) \right] \right\}^{\frac{1}{2D_T}} \cdot t^{\frac{1}{2D_T}} \\ L_\pi = \left\{ \frac{(D_T+D_f-1)(2-D_f)}{D_f w_{\min}^{1-D_T} (1-\phi)} \left[ \frac{p_o}{6\mu} (C_2 + 6L_s A_2) \right] \right\}^{\frac{1}{2D_T}} \cdot t^{\frac{1}{2D_T}} \end{cases} \quad (30)$$

Where  $L_{cp}$  and  $L_\pi$  are the imbibition lengths of clay pores under capillary force and osmotic pressure, respectively.

Combined with the imbibition pore area of clay minerals, the pore imbibition volume is:

$$V_{imc} = A\phi_{tc} L_c \quad (31)$$

Where  $V_{imc}$  is the imbibition volume of clay pores and  $\phi_{tc}$  is the porosity when accounting for the contribution from clay pores.

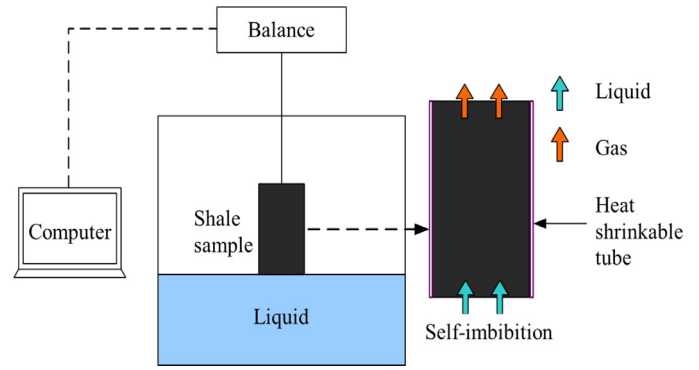


Fig. 7. Schematic of shale imbibition experiment setup.

According to the shale multi-porosity splitting model [51], the cumulative imbibition volume  $V_{im}$  is the sum of imbibition volumes of organic pores, brittle mineral pores, and clay pores:

$$V_{im} = V_{imo} + V_{imb} + V_{imc} \quad (32)$$

Where  $V_{im}$  is the total imbibition volume.

### 3.3. Validation and analysis

A shale core of the Longmaxi formation at Sichuan Basin in China was utilized in our self-imbibition experiment with distilled water as wetting fluid. A schematic of the experiment setup can be found in Fig. 7, coupling with specific measuring methods for modeling parameters, such as many physical and chemical properties.

The experimental procedure is summarized as the following five steps:

- (1) Prepare a standard shale core of 5.0 cm in length and measure the basic parameters (Table 3 and 4).
- (2) Dry the core by placing the core in an oven and heat it for more than 10 h at a temperature of 100 °C.
- (3) Weigh the core and wrap the core surface with a heat shrinkable tube.
- (4) Position the shale core into the imbibition experiment setup, as shown in Fig. 7.
- (5) Monitor weight change of the core through the whole imbibition process.
- (6) Carry out the same drying treatment in the end.

From the experimental results, a logarithmic curve of imbibition volume versus time can be plotted in Fig. 8a. Meanwhile, using the measured parameters shown in Table 3 and 4 for the model given by Eq. (32), we can calculate the imbibition volume as a function of imbibition time too, see Fig. 8b. Note that in our model neither pore structure change nor induced micro-fractures are taken into account aiming to simplify our models as much by using less parameters.

It is evident that the experimental imbibition process can be divided into three major stages according to the slopes of the three linear functions, and the three stages can be explained in physics as follows.

Stage 1: It is a procedure during which only self-imbibition occurs and no pore microstructure changes are involved, and no micro-fractures are created. According to the theoretical imbibition flow process in shale rock, the imbibition volume under the condition of fixed pore morphology can be described as a linear function of imbibition time, which is confirmed by the trendline shown in Fig. 8a with a big coefficient of determination of 0.9983. At this stage, the proposed model is able to set exactly the same condition, consequently achieve an excellent agreement with the exper-

**Table 3**  
Parameters of the shale core sample.

Parameter	Unit	Organic pore	Brittle pore	Clay pore	Measuring method
$\theta$	°	80.40	16.20	11.50	Cassie and Baxter method [52]
$\Phi$ (mineral porosity)	%	20.08	0.88	7.84	Wang et al. method [51]
$m$	-	2.336	3.286	-	FESEM
$L_s$	nm	4.41	1.56	1.53	Contact Angle fitting
$b_{max}$	nm	627	1020	461	FESEM
$b_{min}$	nm	1.47	7.5	1.47	FESEM
$D_f$	-	2.681	2.549	2.619	FESEM
$D_T$	-	1.212	1.297	1.255	Hager et al. method [53]
$\Phi_t$ (core porosity)	%	1.534	0.676	1.600	Helium test

**Table 4**  
The essential parameters of the shale sample and the wetting fluid.

Parameter	Af	$\mu$	$\sigma$	$C_{sh}$	$C_f$
Unit	cm <sup>2</sup>	mPa•s	mN/m	mol/L	mol/L
Value	6.45	1.00	74.10	0.525	0.017
Measuring method	Experimental measurements	Viscometer test	Surface tension meter	Chromatograph test	Formula calculation
Parameter	T	ECEC	$R_{ca-m}$	$R_{ca-w}$	$R_{a-mw}$
Unit	K	-	-	-	-
Value	293.15	3.7	1.8	1.63	1.37
Measuring method	Thermometer test	Methylene blue test	Constant	Constant	Regressive calculation

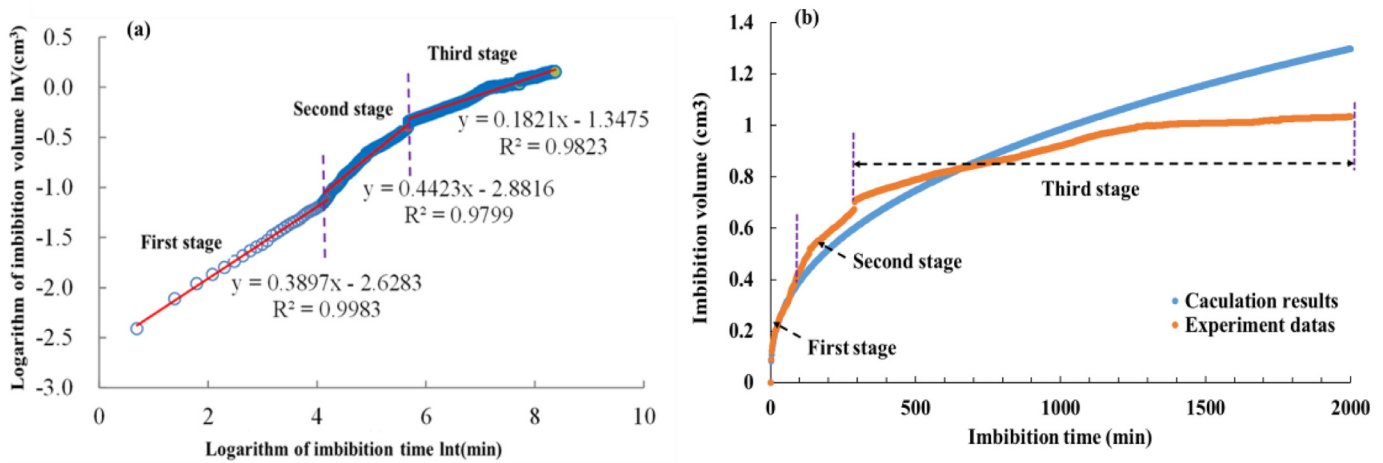


**Fig. 8.** (a) The double logarithmic dotted curve of experimental imbibition volume against time with three linear trendlines, (b) comparison between experimental data and model calculated results.

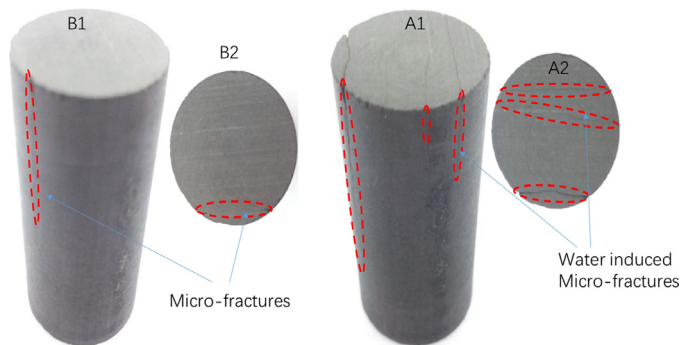


**Fig. 9.** Experimental observation of micro-fractures induced during the second stage.

iment, in other words it is successful in our model simulation of the imbibition process regarding multiple types of shale pores.

Stage 2: During this period, micro-fractures are gradually induced and opened up (see Fig. 9) and pores are slightly expanded too, which was confirmed by Liu & Sheng [54] as well, due to water absorption into shale matrix. As a result, the linear correlation

between imbibition volume and time begins to fail. As the model does not take into account any pore structure evolution, so it is expected that the model estimated volume is less than the experimental observation (Fig. 8b).

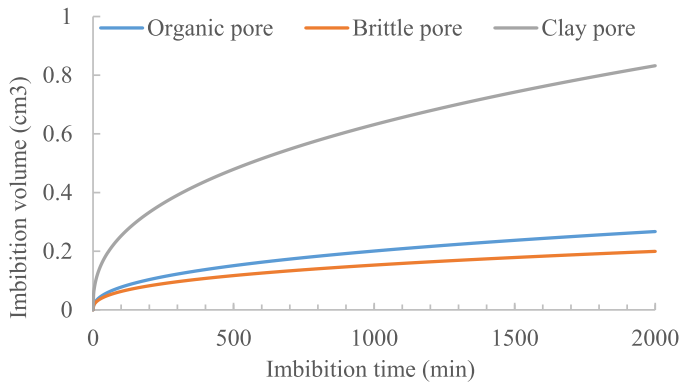
Stage 3: The experimental imbibition water started at a moment beyond 1500 min to grow slowly and even stop near the end as the core sample has limited length and gets water-saturated quickly. If we do utilize linear relationships to approximate the complete data produced during the three stages, see Fig. 8a, it is clear that the three slopes are distinct to each other. Note that at this last stage, the calculated value is about 8%–30% higher than the experimental result (Fig. 8b) and has a trend to increase persistently, which is obviously contrast to the experimental tendency. This is because the core sample in the experiment has limited length but the “sample” length considered in our model is unlimited, i.e., there is no chance for the modeling sample to get water-saturated, hence the model calculated volume goes up the way as shown in Fig. 8b.

Fig. 10 compares the imbibition volumes against imbibition time for the three types of pores. With the model parameters shown in Tables 3 and 4, note that the maximum imbibition volume of clay pores is 0.832cm<sup>3</sup>, which accounts for 64% of the to-

**Table 5**  
The parameters value of the non-clay pores in shale.

Parameter	$\theta$	$\mu$	$\sigma$	$L_s$	$m$	$D_f$	$D_T$	$b_{max}$	$b_{min}$	$b_{av}^*$	$\Phi$
Unit	$^\circ$	$mPa\cdot s$	$mN/m$	$nm$	-	-	-	$nm$	$nm$	$nm$	%
Value	30	1	70	5	4	2.62	1.269	897	1.49	3.98	4.83

\* Mean pore short axis.



**Fig. 10.** Comparison curve of calculation results of imbibition of three types of pores.

tal volume, followed by further imbibition amount of 0.267 cm<sup>3</sup> within organic pores, for 20.6%, and ceased at 0.2 cm<sup>3</sup> imbibition volume of brittle pores, for 15.4%.

#### 4. Imbibition influencing factors

The imbibition model of clay and non-clay pores can be expressed in the form of a shale fractal imbibition model:

$$V = C_{imV}t^{1/(2D_T)} = A_{im}C_{imL}t^{1/(2D_T)} \quad (33)$$

Where  $V$  is the imbibition volume,  $C_{imL}$  is the length imbibition coefficient (imbibition length at  $t = 1$ ) and  $C_{imV}$  is the volume imbibition coefficient (imbibition volume at  $t = 1$ ).

In Eq. (33), the time index (i.e.,  $1/2D_T$ ) is less than 0.5, which is associated with fractal characteristics and pore connectivity of shale pores. It is consistent with the range of 0.1 and 0.5 obtained by Yang et al. [55] and Singh [19] through shale imbibition experiments. When it is 1, the model becomes a uniform bundle model, and the imbibition time index is 0.5.

The imbibition coefficients ( $C_{imL}$  and  $C_{imV}$ ) reflect the potential of shale pores for imbibition; the higher their value, the stronger the imbibition capacity.  $C_{imL}$  refers to imbibition depth or length, and  $C_{imV}$  quantifies the imbibition volume. As indicated by Eq. (33), the imbibition volume will be greater for longer imbibition times and larger imbibition areas.

##### 4.1. Fractal analysis of imbibition in non-clay pores

To explore the factors that affect imbibition capacity of non-clay pores, a list of all the parameters that are directly or indirectly used as input to Eq. (33) is compiled in Table 5. The presented values will be used in evaluating the sensitivity of the imbibition process when pore fractal characteristic, pore size and porosity are allowed to vary, while keeping all the other elements constant.

###### 4.1.1. Effect of pore fractal characteristics

Pore fractal characteristics include pore and tortuosity fractal dimensions. Considering Eq. (33) and the data given in Table 3, the length imbibition coefficients are computed (Fig. 11). With the

**Table 6**  
The parameters value of the clay pores in shale.

Parameter	$\theta$	$w_{max}$	$w_{min}$	$L_s$	$E_{CEC}$	$D_f$	$D_T$
Unit	$^\circ$	$nm$	$nm$	$nm$	$mmol/100 g$	-	-
Value	11.5	261	1.49	1.53	3.7	2.62	1.377
Parameter	$C_{sh}$	$R_{ca-m}$	$R_{ca-w}$	$R_{a-mw}$	$C_f$	$\Phi_c$	$T$
Unit	$mol/L$	-	-	-	$mol/L$	%	$K$
Value	0.87	1.8	1.63	1.37	0.017	7.84	423.15

increase of the pore fractal dimension, the length imbibition coefficient decreases gradually (Fig. 11a), which results in the decrease of the imbibition coefficient. This is because the larger the pore fractal dimension is, the higher the number of small pores accounts for [56], further leading to a lower short-axis mean value of elliptic pores.

As the fractal dimension of tortuosity is increased from 1 to 1.5 (Fig. 11b), the length imbibition coefficient experiences a rather sharp fall in a concave manner. This can be anticipated, as a higher level of tortuosity in the flow channels would lead to shorter flow distances.

##### 4.1.2. Effect of pore size

Fig. 12 shows the impact of the maximum ( $b_{max}$ ) and minimum ( $b_{min}$ ) values of short axis on the imbibition coefficient. The length imbibition coefficient is positively correlated with both variables, with  $b_{max}$  causing a greater change.

##### 4.1.3. Effect of porosity

A comparison is drawn between how changing porosity would affect the length and volume imbibition coefficients in Fig. 13a linear relationship is evident in the case of the length imbibition coefficient; while the volume imbibition coefficient follows a power-law trend. It is recognized that higher porosity is associated with smaller tortuosity, meaning a straighter streamline and easier flow. Moreover, the enlarged imbibition area (with higher porosity values) will certainly result in a rising volume imbibition coefficient.

#### 4.2. Fractal analysis of imbibition in clay pores

The list of the measurements relevant to clay pores is given in Table 6. These values are input to the model Eq. (33) to analyze the sensitivity of the imbibition process on clay pore fractal characteristic, pore size and fluid viscosity, meanwhile keeping all the other variables invariant.

##### 4.2.1. Effect of pore fractal characteristics of clay

Similar to non-clay pores, the effects of pore and tortuosity fractal dimensions are investigated and depicted in Fig. 14. Overall, the trends match those of the non-clay pores. The decrease in the imbibition coefficient is sharper for the tortuosity dimension. Once again, the range of values spanned by the osmotic-pressure imbibition is greater, compared to capillary imbibition.

##### 4.2.2. Effect of pore size

Fig. 15 demonstrates how minimum and maximum pore width can change the capillary and osmotic pressure components of the

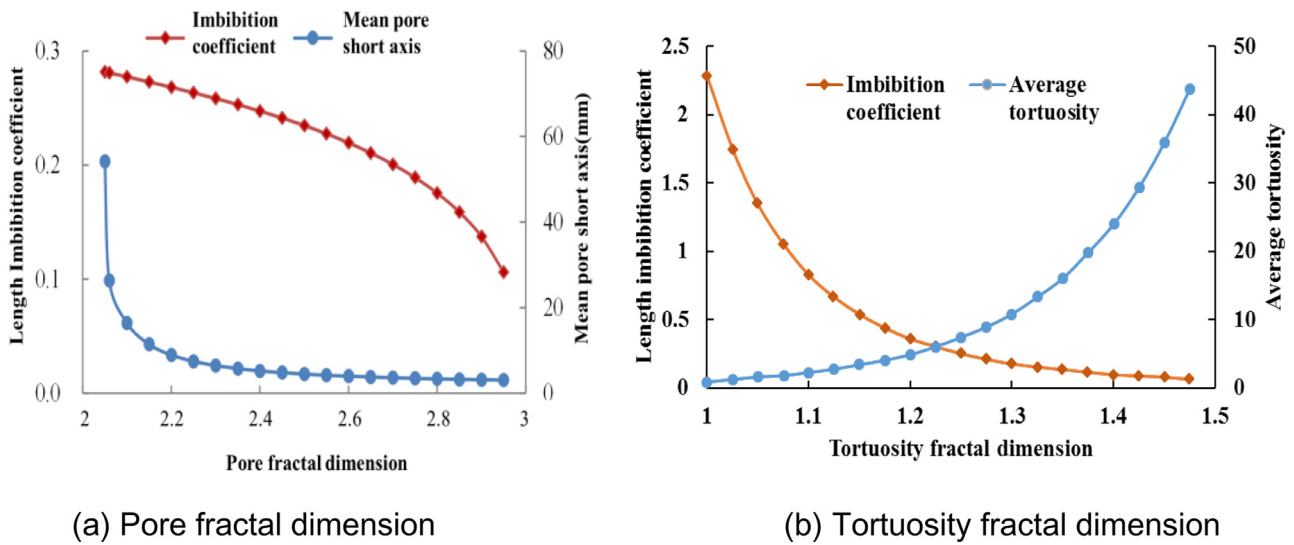


Fig. 11. Imbibition coefficient vs. pore fractal characteristics in non-clay pores. (a) Pore fractal dimension (b) Tortuosity fractal dimension.

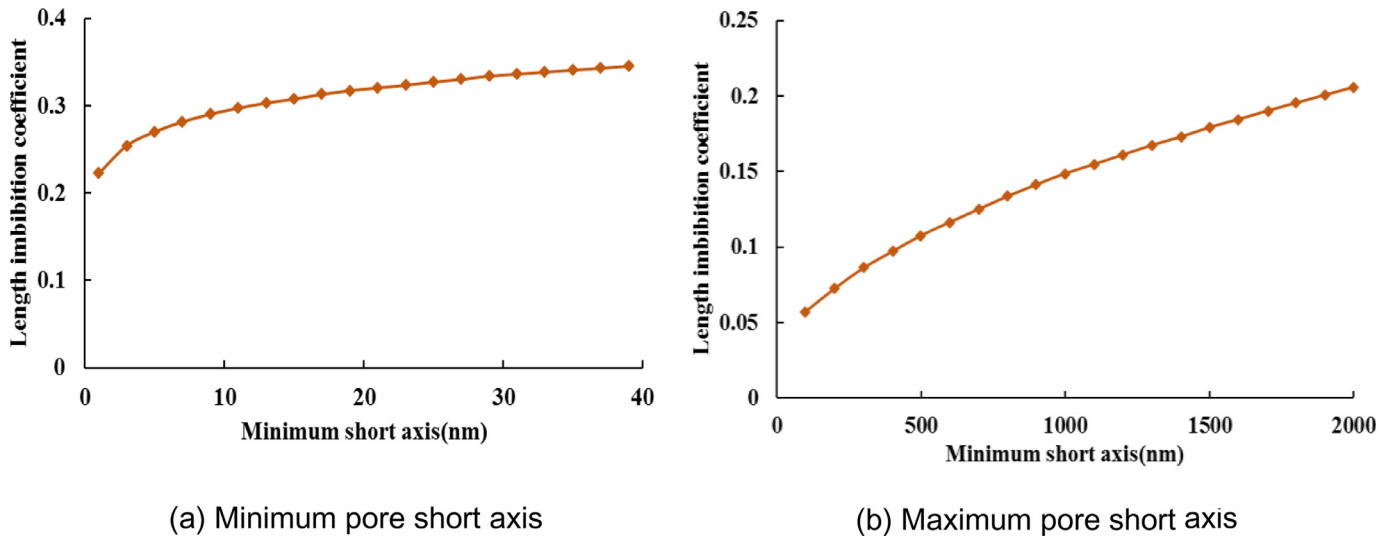


Fig. 12. Length imbibition coefficient vs. non-clay pore size. (a) Minimum pore short axis (b) Maximum pore short axis.

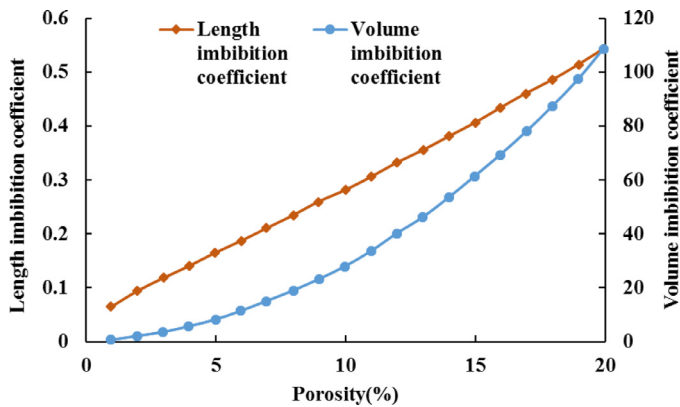


Fig. 13. Length and volume imbibition coefficients vs. porosity of non-clay pores.

$w_{max}$  has produced a steeper and more linear change to the imbibition coefficient (Fig. 15b). The coefficient tends to plateau towards the upper values of  $w_{min}$  (Fig. 15a). Additionally, the increment of imbibition coefficient under osmotic pressure is greater than that from the capillary force.

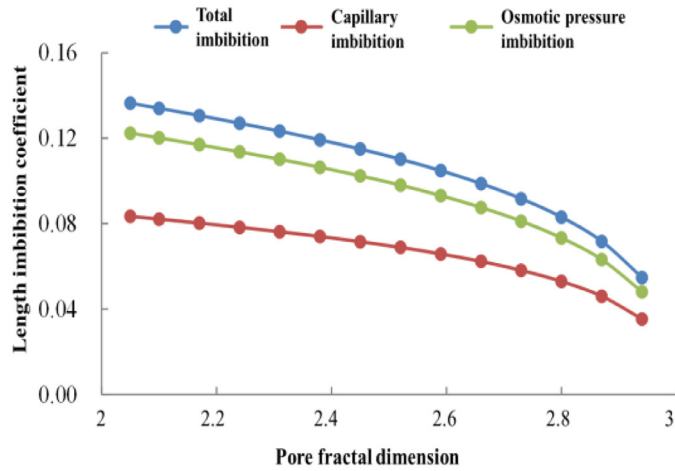
#### 4.2.3. Effect of fluid viscosity

As indicated by Fig. 16, fluid viscosity can play a role in determination of the imbibition coefficient. Viscosity is a measure of the flow capacity of a fluid and can similarly influence the flow driven by either the osmotic pressure or the capillary forces. A dramatic drop in the imbibition coefficient is recorded as viscosity is changed from minimal to around 15 mPa·s. Beyond this value, the imbibition begins to gradually stagnate. This inverse relationship is described by Eq. (30).

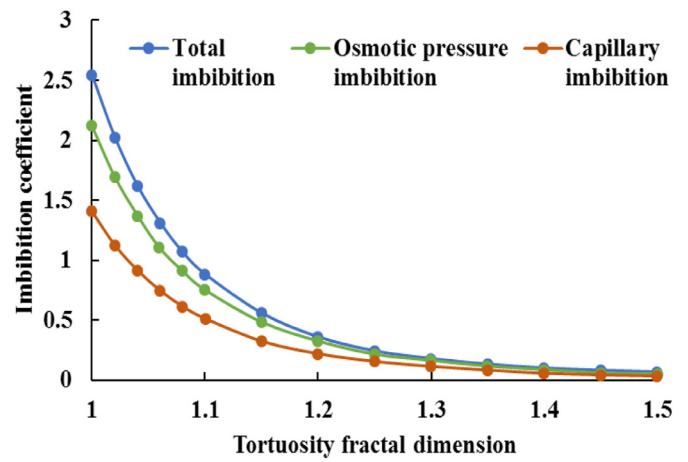
#### 4.3. Comparing the imbibition capacity of the three pore types

Based on the discussions above, it should be obvious that shale imbibition is determined by all of the organic, brittle mineral and

imbibition as well as total imbibition. The length imbibition coefficient has a positive correlation with both  $w_{min}$  and  $w_{max}$ ; however,

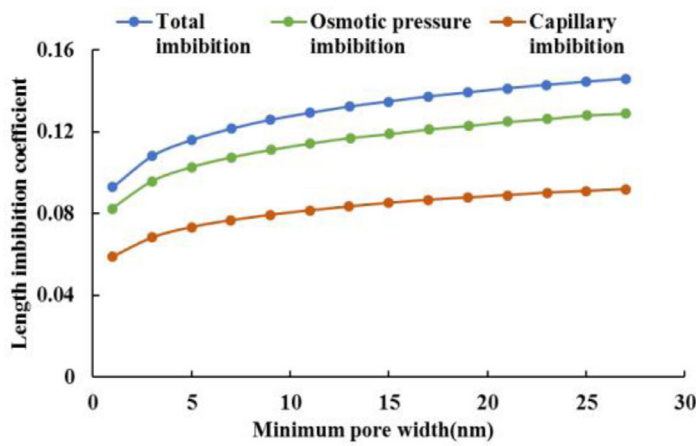


(a) Pore fractal dimension

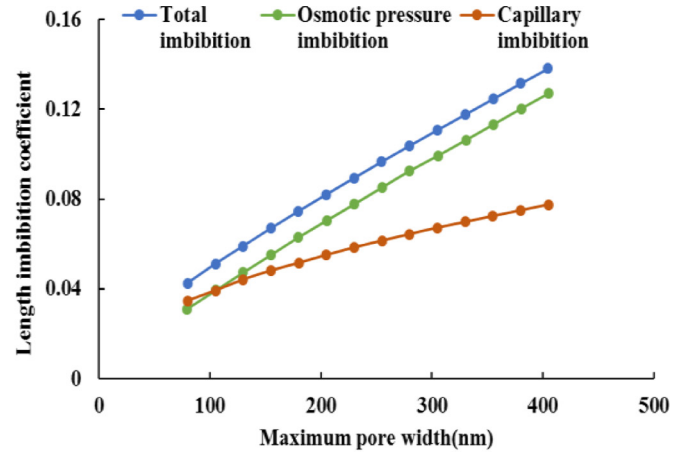


(b) Tortuosity fractal dimension

Fig. 14. Length imbibition coefficient vs. fractal characteristics in clay pores. (a) Pore fractal dimension (b) Tortuosity fractal dimension.



(a) Minimum crack width



(b) Maximum crack width

Fig. 15. Length imbibition coefficient vs. minimum and maximum pore size in clay pores. (a) Minimum crack width (b) Maximum crack width.

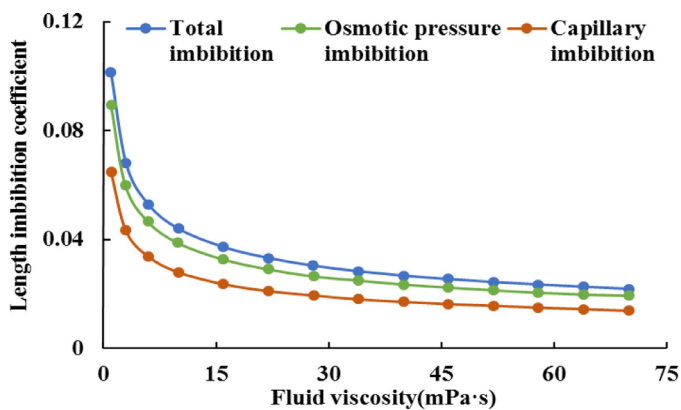


Fig. 16. Imbibition coefficients vs. fluid viscosity in clay pores.

clay pores. The imbibition relationship (Eq. (33)) was used to calculate the imbibition volume. Table 3 provides the characteristic parameters for the three pore types.

#### 4.3.1. Imbibition length comparison

Imbibition length is calculated per pore type and at different times using the information presented in Table 3 and Eq. (33). Results reveal that the clay pores and organic pores have the highest and lowest values of the length imbibition coefficient, respectively, with brittle mineral pores lying in between (Fig. 17a). The same order is observed with regard to the imbibition speed (Fig. 17b). The imbibition length of clay pores is the largest, while that of organic pores is the smallest.

#### 4.3.2. Imbibition volume comparison

The same analysis as above is performed for the imbibition volume. As shown in Fig. 18b, at 1000 min the imbibition volume through clay, brittle mineral and organic pores are 0.631, 0.153 and 0.201cm<sup>3</sup>, respectively. The ultimate imbibition volume via clay pores is considerably larger than the combined volumes of the other two types put together. This is confirmed by the significantly higher value of the volume imbibition coefficient in clay pores (Fig. 18a).

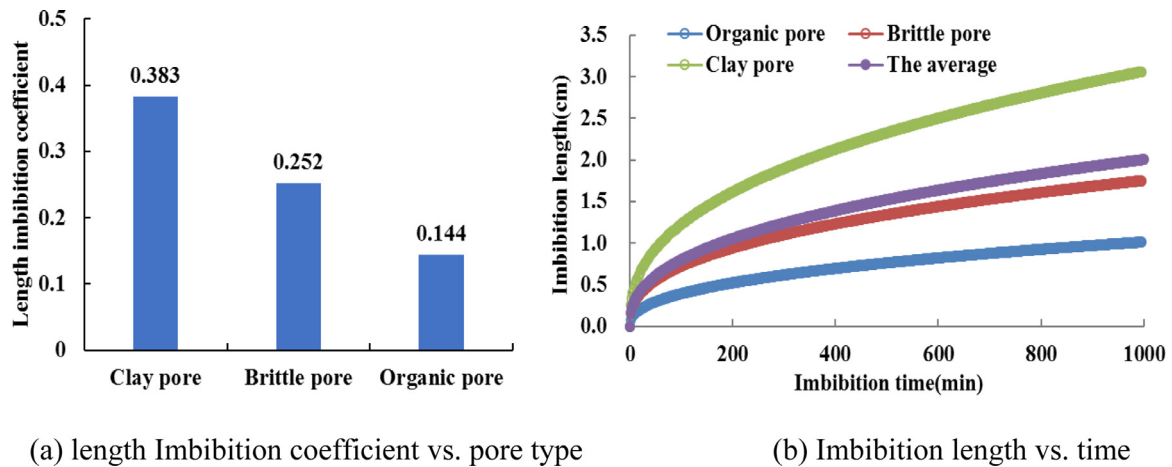


Fig. 17. Comparison of length imbibition of different pore type at various times. (a) length Imbibition coefficient vs. pore type (b) Imbibition length vs. time.

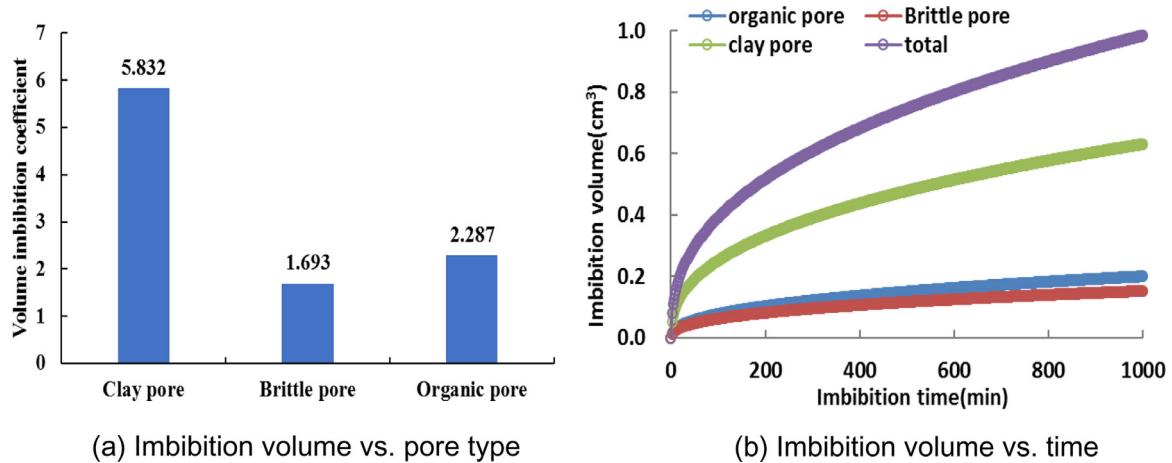


Fig. 18. Comparison of imbibition volume of different pore type at various times. (a) Imbibition volume vs. pore type (b) Imbibition volume vs. time.

### 4.3.3. Discussion

In the comparative analysis of the self-imbibition in three different types of shale pores, it is noticeable that the clay pores self-imbibition depth is deepest, while the organic pores have the shallowest depth. The self-imbibition process cannot be described by piston-like displacement but non-uniform advance instead. This is because apart from the capillary force, the clay pores are also affected by osmotic pressure, which explains why the clay pores have the deepest self-imbibition depth (Fig. 16b). According to Eq. (6), the larger the contact angle the smaller the capillary force. Therefore, the self-imbibition force of organic pores is weakest due to their largest contact angle (Table 3), leading to the shallowest self-imbibition length. Of course, pore size, fractal dimension and tortuosity fractal dimension also have certain amount of influence on the self-imbibition, however in our experiment these parameters have no significant impact to be observed, consequently they are ignored in our model for simulating the self-imbibition in the three kinds of shale pores.

### 5. Conclusion

- (1) The average shale pore sizes are distributed over a wide range from 10 to 200 nm in this work. The organic and clay pores account for the largest proportion in the range of 10–30 nm, while brittle mineral pores are most frequently at diameters in the range of 100–200 nm. Organic and brittle mineral pores are

geometrically more or less elliptic, whereas the clay pores resemble parallel fractures.

- (2) The effect of fractal characteristics on imbibition capacity of clay and non-clay pores is nearly identical. With increase in the fractal dimensions of pores and tortuosity, the imbibition capacity drops, but a more significant effect in the case of tortuosity. As the pore fractal dimension approaches values close to the upper limit of 2, the water absorption capacity decreases even more significantly.
- (3) The relationship between clay and non-clay pore size and imbibition is also consistent and straightforward. In both cases, the enhancement of imbibition is greater when the maximum equivalent diameter (short axis for non-clay pores and crack width for clay pores) is greater. For clay pores, the increase of imbibition capacity under osmotic pressure is greater than that under capillary force.
- (4) When the liquid viscosity is incremented up to a certain value (e.g., 15 mPa.s in this work), the imbibition coefficient of clay pores undergoes a severe drop (under either osmotic pressure or capillary forces). Beyond this critical value, the imbibition begins to gradually stagnate.
- (5) Among the three pore types, clay pores have the fastest imbibition and the longest imbibition length. Moreover, the imbibition volume of clay pores is much larger than that of organic and brittle mineral pores.

## Declaration of Competing Interest

The authors declare that they have no known competing financial interests or personal relationships that could have appeared to influence the work reported in this paper.

## Acknowledgement

The authors acknowledge that this work was successfully completed through the financial support of the National Natural Science Foundation of China (project No. 51525404).

## References

- Mirchi V, Saraji S, Goual L, et al. Dynamic interfacial tension and wettability of shale in the presence of surfactants at reservoir conditions. *Fuel* 2015;148:127–38.
- Yuan B, Wang Y, Zeng S. Effect of slick water on permeability of shale gas reservoirs. *J Energy Resour Technol* 2018;140:112901–7.
- Zhang S, Xian X, Zhou J, et al. Experimental study of the pore structure characterization in shale with different particle size. *J Energy Resour Technol* 2018;140:054502–11.
- Yuan B, Wang Y, Wei N. The effects of fracturing fluid retention on permeability of shale reservoirs. *Energy Procedia* 2019;158:5934–9.
- Chong HA, Robert D, John YW. Modeling of hydraulic fracture propagation in shale gas reservoirs: a three-dimensional, two-phase model. *J Energy Resour Technol* 2017;139:2903–12.
- Guo T, Li Y, Ding Y, et al. Evaluation of acid fracturing treatments in shale formation. *Energy Fuels* 2017;31:10479–89.
- Vincent MC. The next opportunity to improve hydraulic-fracture stimulation. *J Petrol Technol* 2012;64:118–27.
- He Y, Cheng S, Li S, et al. A semianalytical methodology to diagnose the locations of underperforming hydraulic fractures through pressure-transient analysis in tight gas reservoir. *SPE J* 2017;22:924–39.
- Nasriani HR, Jamiolahmady M. Flowback cleanup mechanisms of post-hydraulic fracturing in unconventional natural gas reservoirs. *J Nat Gas Sci Eng* 2019;66:316–42.
- Sun J, David S. Investigating the effect of improved fracture conductivity on production performance of hydraulic fractured wells through field case studies and numerical simulations. *J Can Pet Technol* 2015;54:442–9.
- Hull NM, Rosenblum JS, Robertson CE, et al. Succession of toxicity and microbiota in hydraulic fracturing flowback and produced water in the Denver–Julesburg Basin. *Sci Total Environ* 2018;644:183–92.
- Abbasi M, Dehghanpour H, Hawkes RV. Flowback analysis for fracture characterization. In: *SPE Canadian unconventional resources conference*. Society of Petroleum Engineers; 2012. p. 23.
- Ghanbari E, Dehghanpour H. The fate of fracturing water: a field and simulation study. *Fuel* 2016;163:282–94.
- Clarkson CR, Qanbari F. An approximate semianalytical multiphase forecasting method for multifractured tight Light–Oil wells with complex fracture geometry. *J Can Pet Technol* 2015;54:489–508.
- Cai J, Yu B. Advances in studies of spontaneous imbibition in porous media. *Advances in Mechanics* 2012;42:735–54.
- King GE. Hydraulic Fracturing 101: what every representative, environmentalist, regulator, reporter, investor, university researcher, neighbor and engineer should know about estimating frac risk and improving frac performance in unconventional gas and oil wells. In: *SPE hydraulic fracturing technology conference*. Society of Petroleum Engineers; 2012. p. 80.
- Perapon F, Torcuk MA, Wallace J, et al. Managing shut-in time to enhance gas flow rate in hydraulic fractured shale reservoirs: a simulation study. In: *SPE annual technical conference and exhibition*. Society of Petroleum Engineers; 2013. p. 13.
- Nicot JP, Scanlon BR. Water use for shale-gas production in Texas. *U.S. Environ Sci Technol* 2012;46:3580–6.
- Singh H. A critical review of water uptake by shales. *J Nat Gas Sci Eng* 2016;34:751–66.
- Handy LL. Determination of effective capillary pressures for porous media from imbibition data. Society of Petroleum Engineers; 1960. SPE 1361.
- Li K, Horne RN. Characterization of spontaneous water imbibition into gas-saturated rocks. *SPE/AAPG Western regional meeting Long Beach, California, USA*. SPE 62552; 2001.
- Li K, Horne R. An analytical scaling method for spontaneous imbibition in gas/water/rock systems. *SPE J* 2004;9(9):322–9.
- Cheng Z, Ning Z, Wang Q, et al. The effect of pore structure on non-Darcy flow in porous media using the lattice Boltzmann method. *J Petroleum Sci Eng* 2019;172:391–400.
- Cai J, Yu B, Zou M, et al. Fractal characterization of spontaneous co-current imbibition in porous media. *Energy Fuels* 2010;24:1860–7.
- Jiang F, Chen D, Chen J, et al. Fractal analysis of shale pore structure of continental gas shale reservoir in the Ordos Basin, NW China. *Energy Fuels* 2016;30(6):4676–89.
- Li K, Zhao H. Fractal prediction model of spontaneous imbibition rate. *Transp Porous Media* 2012;91(2):363–76.
- Lucas R. Ueber das Zeitgesetz des kapillaren. Aufstiegs von Flüssigkeiten. *Kolloid-Zeitschrift* 1918;23:15–22.
- Washburn EW. The dynamics of capillary flow. *Phys Rev* 1921;17(3):273–83.
- Zhmud BV, Tiberg F, Hallstenson K. Dynamics of capillary rise. *J Colloid Interface Sci* 2000;228(2):263–9.
- Fries N, Dreyer M. An analytic solution of capillary rise restrained by gravity. *J Colloid Interface Sci* 2008;320(1):259–63.
- Benavente D, Lock P, Cura MAGD, et al. Predicting the capillary imbibition of porous rocks from microstructure. *Transp Porous Media* 2002;49(1):59–76.
- Dimitrov DI, Milchev A, Binder K. Capillary rise in nanopores: molecular dynamics evidence for the Lucas–Washburn equation. *Phys. Rev. Lett.* 2007;99(5):54501.
- Chalmers GR, Bustin RM, Power I M. Characterization of gas shale pore systems by porosimetry, pycnometry, surface area, and field emission scanning electron microscopy/transmission electron microscopy image analyses: examples from the Barnett, Woodford, Haynesville, Marcellus, and Doig unit. *Am Assoc Pet Geol Bull* 2012;96(6):1099–119.
- Gu X, David RC, Gernot R, et al. Pores in marcellus shale: a neutron scattering and FIB–SEM study. *Energy Fuels* 2015;29(3):1295–308.
- Liu W, Liu J, Cai M, et al. Pore evolution characteristic of shale in the Longmaxi Formation. *Sichuan Basin Petroleum Res* 2017;2(4):291–300.
- Wang Y, Jiang H, Ke Y, et al. Investigation of pore structures in shallow Longmaxi Shale, South China. via Large-Area Electron Imager Neutron Scatter Techniques. *Energy Fuels* 2020;34(7):7974–84.
- Chen Q, Zhang J, Tang X, et al. Relationship between pore type and pore size of marine shale: an example from the Sinian–Cambrian formation, upper Yangtze region, South China. *Int J Coal Geol* 2016;158:13–28.
- Kuila U, Prasad M. Specific surface area and pore-size distribution in clays and shales. *Geophys Prospect* 2013;61:341–62.
- Wang S, Javadpour F, Feng Q. Molecular dynamics simulations of oil transport through inorganic nanopores in shale. *Fuel* 2016;171:74–86.
- Joseph P, Tabeling P. Direct measurement of the apparent slip length. *Phys Rev E Statistic Nonlinear Soft Matter Phys* 2005;71(3 Pt 2A):035303.
- Wang X, Zhang X, Meng Y, et al. Experimental study of boundary slip in confined liquids in micro/nano scale systems and the effect of interfacial wetting. *J Tsinghua Univ (Sci Technol)* 2008;48(8):1302–5.
- Wu K, Chen Z, Li J, et al. Wettability effect on nanoconfined water flow. *Proc Natl Acad Sci USA*. 2017;114(13):3358–63.
- Javadpour F, McClure M, Naraghi ME. Slip-corrected liquid permeability and its effect on hydraulic fracturing and fluid loss in shale. *Fuel* 2015;160:549–59.
- Yu B, Cheng P. A fractal permeability model for bi-dispersed porous media. *Int J Heat Mass Transf* 2002;45:2983–93.
- Schechter DS, Zhou D, FMO Jr. Low IFT drainage and imbibition. *J Pet Sci Eng* 1994;11:283–300.
- Li K. More general capillary pressure and relative permeability models from fractal geometry. *J Contam Hydrol* 2010;111:13–24.
- Yu BM, Cai JC, Zou MQ. On the physical properties of apparent two-phase fractal porous media. *Vadose Zone J* 2009;8:177–86.
- Neuzil CE, Provost AM. Recent experimental data may point to a greater role for osmotic pressures in the subsurface. *Water Resour Res* 2009;45(3):450–5.
- Fritz SJ, Marine IW. Experimental support for a predictive osmotic model of clay membranes. *Geochim. Cosmochim. Acta* 2001;47(8):1515–22.
- Choi C, Westin J, Breuer K. Apparent slip in hydrophilic and hydrophobic microchannels. *Phys Fluids* 2003;15:2897–902.
- Wang Y, Huang J, Li X, et al. Quantitative characterization of fractures and pores in shale beds of the Lower Silurian, Longmaxi Formation, Sichuan Basin. *Natural Gas Ind* 2015;35:8–15.
- Cassie ABD, Baxter S. Wettability of porous surfaces. *Trans Faraday Soc* 1944;40:546–51.
- Hager J, Hermansson M, Wimmerstedt R. Modelling steam drying of a single porous ceramic sphere: experiments and simulations. *Chem Eng Sci* 1997;52(8):1253–64.
- Liu K, Sheng JJ. Experimental study of the effect of stress anisotropy on fracture propagation in eagle ford shale under water imbibition. *Eng Geol* 2019;249:13–22.
- Yang L, Ge H, Shi X, et al. The effect of microstructure and rock mineralogy on water imbibition characteristics in tight reservoirs. *J Nat Gas Sci Eng* 2016;34:1461–71.
- Yang R, He S, Yi J, et al. Nano-scale pore structure and fractal dimension of organic-rich Wufeng–Longmaxi shale from Jiaoshiba area, Sichuan Basin: investigations using FE–SEM, gas adsorption and helium pycnometry. *Mar Pet Geol* 2016;70:27–45.